RSC Advances

PAPER

View Article Online
View Journal | View Issue

Cite this: *RSC Adv.*, 2021, **11**, 18565

A photosensitive metal–organic framework having a flower-like structure for effective visible light-driven photodegradation of rhodamine B†

Lu Qin, Shicheng Zhao, * Chenran Fan and Qian Ye

Porphyrin-based metal–organic frameworks (MOFs) have great photocatalytic potential due to their good photosensitivity. Their photocatalytic performance is not only determined by molecular structure but also by morphology. Flower-like MOFs are considered to be good materials for catalysis due to their larger specific surface area, more exposed active sites, and good stability. Here, we first proposed a method to synthesize flower-like porphyrin-based MOFs using trifluoroacetic acid as a morphology control agent. These MOFs had a large BET surface area (605.04 m^2 g^{-1}), a stable structure and a complete morphology. Meanwhile, we discussed their self-assembly process and mechanism in detail. In addition, we studied the photocatalytic performance of flower-like porphyrin-based MOFs and found that the flower-like Cu-TCPP (TCPP = tetrakis(4-carboxyphenyl)porphyrin) has excellent photocatalytic activity. Its photodegradation efficiency toward the cationic dye rhodamine B reached 88% within 100 min and the sample still maintained its stable catalytic activity and complete flower-like morphological structure after five repeated uses. Furthermore, this synthetic strategy can be extended to control the morphology of other MOFs.

Received 8th April 2021
Accepted 12th May 2021

DOI: 10.1039/d1ra02746h

rsc.li/rsc-advances

1. Introduction

Among the synthetic dyes used in the textile and printing industries, azo dyes (*e.g.*, methyl orange, Congo red), thiazide dyes (*e.g.*, methylene blue), and fluorescein dyes [*e.g.*, rhodamine B (RhB)] are the most common.[1,2] Because their resulting toxic dye wastewaters can pollute the environment, it is urgent to develop a method for the treatment of dye wastewater. However, dyes generally have stable molecular structures, are highly color-rendering, are chemically inert (*e.g.*, to light, heat, and catalysts), and are difficult to decompose. Traditional biological and physical treatment methods (*e.g.*, adsorption, ultrafiltration, coagulation)[3,4] and other more advanced degradation processes have several limitations—for example, complex devices/processes or high energy consumption. Accordingly, photocatalysis has become an active area of research due to its high catalytic activity and the use of green energy (natural light).[5–10]

Metal–organic frameworks (MOFs)[11] are crystalline porous materials constructed from organic linkers and metal ions or clusters.[12,13] They have been successfully applied in catalysis, especially in the field of photocatalysis,[14–16] due to high specific surface areas, large porosities, tunable pore sizes, and flexible functionality.[17,18] In particular, the porphyrin-based MOFs have better photothermal stability, better photosensitivity and long-lifetime excited states, and show excellent photoelectric performance, because the porphyrin molecule has large π-conjugated structure with high rigidity and shows good electron mobility. At present, the porphyrin-based MOFs are widely used in photocatalysis[19]—for example, the photocatalytic reduction of CO_2,[20–22] photocatalytic dye degradation,[15,17] photocatalytic hydrolysis producing H_2,[23,24] and the photocatalysis of various organic reactions.[18,25,26]

The morphology of MOFs is another important factor that can greatly affect their performance, especially in the field of catalysis. Among the various types of layered nanostructures, flower-like nanostructures are the most suitable layered nanostructures for catalysis.[27] In particular, flower-like nanostructures assembled from two-dimensional (2D) nanosheets feature interconnected open pores, thereby exposing a large number of active sites and ensuring high catalytic performance.[28,29] Ultrathin 2D nanosheets assembled into flower-like structure in which they in close contact with each other, thereby displaying high stability and reusability.[30] Typically, flower-like

Shanghai Key Laboratory of Multiphase Materials Chemical Engineering, School of Chemical Engineering, East China University of Science and Technology, 130 Meilong Road, Shanghai 200237, China. E-mail: zhaosc@ecust.edu.cn; Tel: +86-21-64252352

† Electronic supplementary information (ESI) available: UV-vis spectra of TCPP and flower-like M-TCPP (M = Cu, Zn and Co), EDS point scan of flower-like Cu-TCPP, thermogravimetric curve of flower-like Cu-TCPP, XRD spectra (a) and FTIR spectra (b) of flower-like Cu-TCPP before and after the photocatalytic experiments, SEM images of flower-like Cu-TCPP before and after the photocatalytic reaction, structure and standard curve of rhodamine B, Tauc plot of the UV-vis DRS spectrum of flower-like Cu-TCPP and VB XPS diagram of flower-like Cu-TCPP. See DOI: 10.1039/d1ra02746h

nanomaterials have higher specific surface areas [Brunauer–Emmett–Teller (BET) surface areas] than those of spherical nanoparticles.[31] Based on the foregoing, flower-like porphyrin-based MOFs should have better photocatalytic performance, but precise control of their morphology to expose more active sites is still a huge challenge. Up to now, the controllable synthesis of flower-like porphyrin-based MOFs have not yet been reported.

In this paper, we report flower-like MOFs self-assembled from 2D nanosheets, synthesized through the coordination of metal ions (mainly Cu^{2+}, Zn^{2+}, and Co^{2+}) to TCPP through a one-step hydrothermal method using suitable morphological control agent. Meanwhile, we analyzed the synthesis process in detail and proposed the mechanism of self-assembly into a flower shape. In addition, experimental investigations found that flower-like porphyrin-based MOFs show high photocatalytic activity, which can effectively photodegrade the cationic dye RhB.

2. Experimental section

2.1 Chemicals

All chemicals were purchased from commercial suppliers and used without further purification, unless otherwise mentioned. Copper nitrate trihydrate [$Cu(NO_3)_2 \cdot 3H_2O$, 99%], zinc nitrate hexahydrate [$Zn(NO_3)_2 \cdot 6H_2O$, 98%], cobaltous nitrate hexahydrate [$Co(NO_3)_2 \cdot 6H_2O$, 98%], and RhB were purchased from Adamas-Beta; tetrakis(4-carboxyphenyl)porphyrin (TCPP, 97%) was purchased from TCI; polyvinylpyrrolidone (PVP; average molecular weight: *ca.* 40 000) and *N*,*N*-dimethylformamide (DMF) were purchased from Sigma-Aldrich; EtOH (99.8%), trifluoroacetic acid (TFA, 99%), formic acid (FA), acetic acid (AA), nitric acid (HNO_3), hydrofluoric acid (HF) and hydrochloric acid (HCl) were purchased from General-Reagent. Ultra-pure water was obtained from a Milli-Q System.

2.2 Flower-like M-TCPP (Cu, Zn, Co)

Taking the synthesis of flower-like Cu-TCPP as an example, the detailed synthesis process is as follows: $Cu(NO_3)_2 \cdot 3H_2O$ (3.6 mg, 0.015 mmol), different acids, and PVP (10.0 mg) were dissolved in a mixture of DMF and EtOH (3 : 1, v/v; 12 mL) in a 20 mL capped vial. A solution of TCPP (4.0 mg, 0.005 mmol) in a mixture of DMF and EtOH (3 : 1, v/v; 4 mL) was added dropwise with stirring. The resulting solution was sonicated for 10 min. Then the vial was heated at 80 °C until the reaction completed. The resulting precipitate was washed twice with EtOH and water, collected by centrifugation (8000 rpm, 10 min), and freeze-dried overnight.

The other flower-like M-TCPP were synthesized using the method described above, except that the metal ion was replaced by Zn^{2+} or Co^{2+} and the molar ratio of the metal ion to the organic ligand TCPP was 3 : 1.

2.3 Characterization

Powder X-ray diffraction (PXRD) patterns were measured using a rotating anode X-ray powder diffractometer (Rigaku) and Cu Kα radiation (λ = 1.54178 Å). Scanning electron microscopy (SEM) images were recorded using a Hitachi S-3400N microscope, equipped with an energy-dispersive X-ray spectroscopy (EDS) system. Field-emission scanning electron microscopy (FESEM) images were recorded using a JSM-6360LV microscope (JEOL). Transmission electron microscopy (TEM) images were recorded using an FEI Talos F200X microscope (Thermo Fisher Scientific, USA), operated at an acceleration voltage of 200 kV; to obtain samples for TEM analysis, Cu-MOFs were subjected to ultrasonic treatment in EtOH and then drops of the ethanolic suspension of the nanosheets were placed onto either holey, carbon-coated, carbon-supported Cu grids or piranha-cleaned Si, and then dried naturally. Attenuated total reflectance Fourier transform infrared spectroscopy (ATR-FTIR) was performed using a Nicolet 6700 instrument. Thermogravimetric analysis (TGA) was performed using a TGA instrument equipped with a furnace and microbalance (PerkinElmer), over the operating temperature range from 30 to 800 °C at a heating rate of 10 °C min^{-1} under a N_2 atmosphere. BET surface areas and pore size distributions were measured using a Micromeritics ASAP 2020 adsorption apparatus, at 77 K and pressures of up to 1 bar; the samples were degassed at 80 °C for 12 h prior to BET measurements. X-ray photoelectron spectroscopy (XPS) was conducted using a Thermo Scientific K-Alpha+ spectrometer equipped with a monochromatic Al Kα X-ray source (1486.6 eV) and operated at 100 W. UV-vis absorption spectra were recorded using a UV 2550 spectrophotometer (PerkinElmer) and QS-grade quartz cuvette (110-QS; Shimadzu). UV-visible diffuse reflectance spectra (UV-vis DRS) of the samples were acquired on a PerkinElmer Lambda 750 spectrophotometer using $BaSO_4$ as the reference with 100% reflectance.

2.4 Photocatalytic activity

The photocatalytic degradation of aqueous RhB solutions was conducted over flower-like Cu-TCPP under irradiation with visible light. A 300 W Xe lamp (PLS-SXE 300) equipped with a 420 nm cut-off filter was used as the light source. Typically, the photocatalyst sample (5 mg) and aqueous RhB solution (10 ppm, 50 mL) were mixed in the photoreactor. The solution was stirred magnetically for 60 min in the dark to achieve the adsorption/desorption equilibrium. Then, a certain amount of H_2O_2 was added to the mixture; the Xe lamp was switched on simultaneously. At scheduled time intervals, aliquots (4 mL) of the sample solution were removed from the reactor and separated through centrifugation. The concentration of RhB remaining in the supernatant solution was calibrated in terms of its maximum absorption at a wavelength of 554 nm, measured using a UV-vis spectrophotometer (UV-2550, Shimadzu).

3. Result and discussion

3.1 Characterization

To synthesize the flower-like M-TCPP (M = Cu, Zn, Co), we selected three organic acids (FA, AA and TFA) and three inorganic acids (HCl, HNO_3 and HF) as morphology control agents.

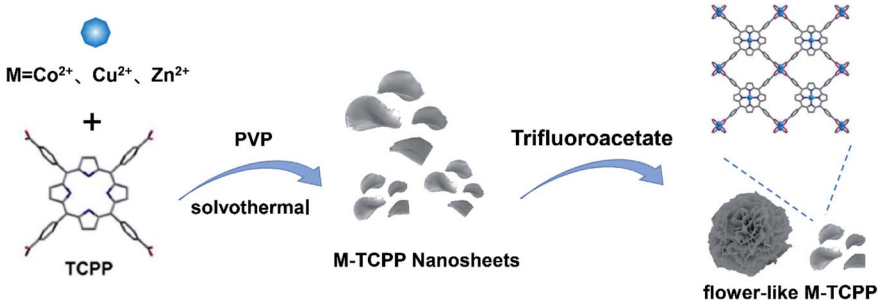

Fig. 1 Schematic representation of the solvothermal method for the preparation of flower-like M-TCPP.

And investigated the effects of various acids on the morphology of Cu-TCPP. The synthesis diagram is shown in Fig. 1.

The Cu-TCPP nanosheet is constructed with Cu-centered TCPP units connected by binuclear $Cu_2(COO)_4$ paddle wheels. The phase purity and crystal structures of the obtained MOFs were determined using XRD. The XRD spectra of Cu-TCPP synthesized with different acids (Fig. 2a) featured four characteristic peaks on the (110), (210), (320) and (440) planes, suggesting that Cu-TCPP had been synthesized successfully, consistent with literature reports.[32,33] In order to prove that we

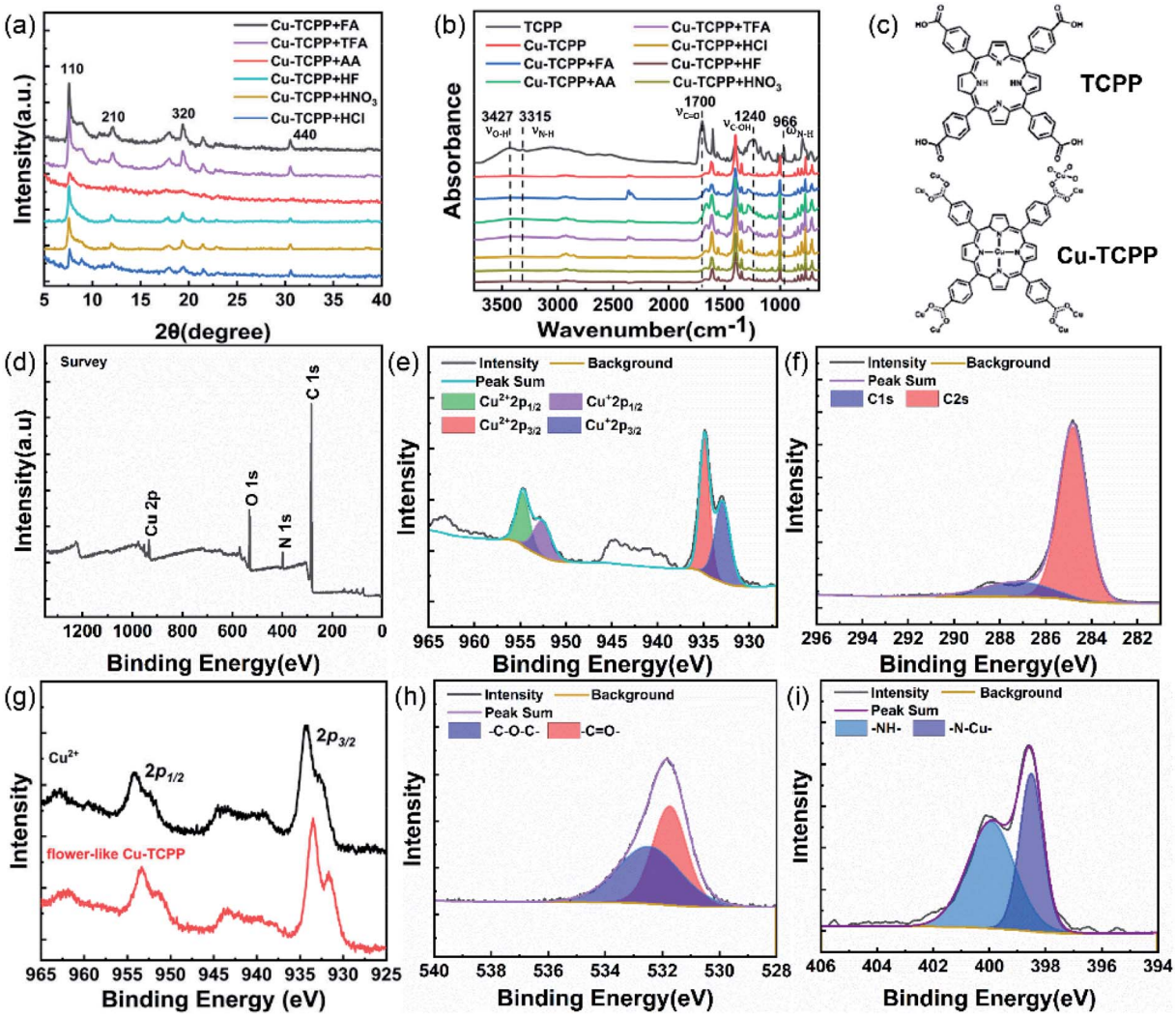

Fig. 2 (a) XRD spectra of Cu-TCPP synthesized in the presence of various acids. (b) FTIR spectra of TCPP and Cu-TCPP. (c) Molecular structures of TCPP and Cu-TCPP. (d)–(f) XPS spectra of flower-like Cu-TCPP: (d) survey, (e) Cu 2p, and (f) C 1s scans. (g) High-resolution Cu 2p XPS spectra of flower-like Cu-TCPP and $Cu(NO_3)_2 \cdot 3H_2O$; (h) O 1s and (i) N 1s scans.

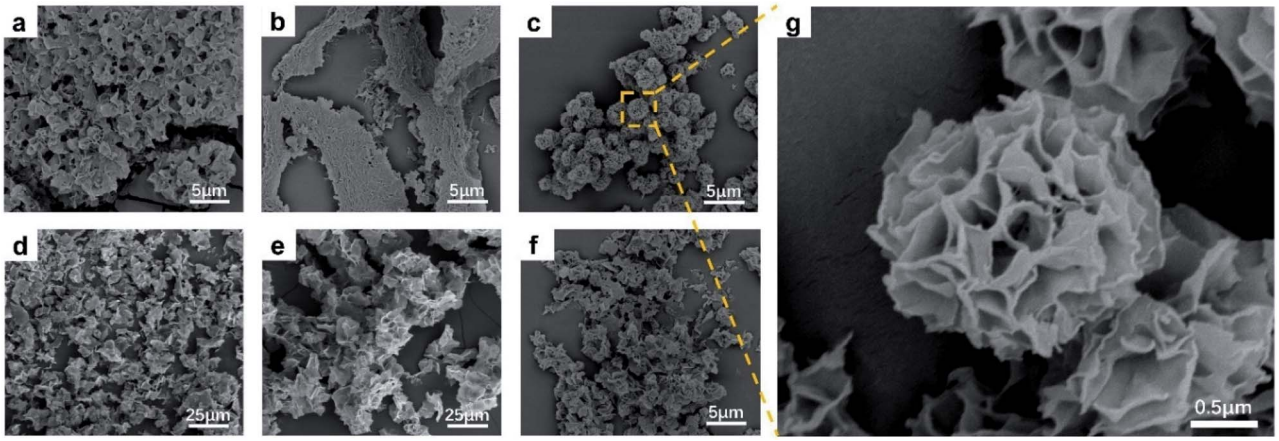

Fig. 3 (a)–(f) SEM images of Cu-TCPP synthesized in the presence of (a) FA, (b) AA, (c) TFA, (d) HF, (e) HNO_3, (f) HCl, each added in an amount of 1.25 μL mL^{-1}. (g) Enlarged SEM image of Cu-TCPP synthesized with TFA.

synthesized the centrally coordinated Cu-TCPP, we performed FTIR characterization on the Cu-TCPP synthesized by adding different acids and the raw material TCPP. As shown in Fig. 2b, the OH stretching at 3427 cm^{-1}, C=O stretching at 1700 cm^{-1}, and C–OH stretching at 1240 cm^{-1}, these three characteristic peaks are attributed to the carboxyl groups on the raw material TCPP. The signals for N–H stretching at 3315 cm^{-1} and N–H out-of-plane rocking at 996 cm^{-1} represented the N–H bonds of the pyrrole rings of TCPP.[34] When Cu^{2+} is coordinated with TCPP to form Cu-TCPP, the characteristic peaks of the carboxyl group of the raw material TCPP and the characteristic peaks of the N–H bond on the pyrrole ring disappear.

The UV-vis spectra (Fig. S1†) of TCPP and M-TCPP (M = Cu, Co, Zn) featured S (strong) and Q (weak) bands having various absorption intensities. The molar extinction coefficient of the porphyrin S band is typically much larger than that of the Q band; accordingly, their absorption intensities were different.[34] Because of the asymmetric chemical environment of the four N atoms in the TCPP ring, the Q-band featured four absorption peaks. When the N atoms of TCPP were coordinated with metal ions, their spatial symmetry increased, the chemical environments of the N atoms became identical, and the intensity of the Q-band absorption signal decreased. Based on the results of XRD, FTIR and UV-vis, we successfully synthesized Cu-TCPP with metalized porphyrin center.

In addition, we used XPS to study the compositions and chemical states of the various Cu-TCPP derivatives. The survey scan spectra (Fig. 2d) revealed that the Cu-TCPP samples were composed of C, N, O, and Cu atoms; EDS scans provided consistent results (Fig. S2†). High-resolution Cu 2p XPS spectra

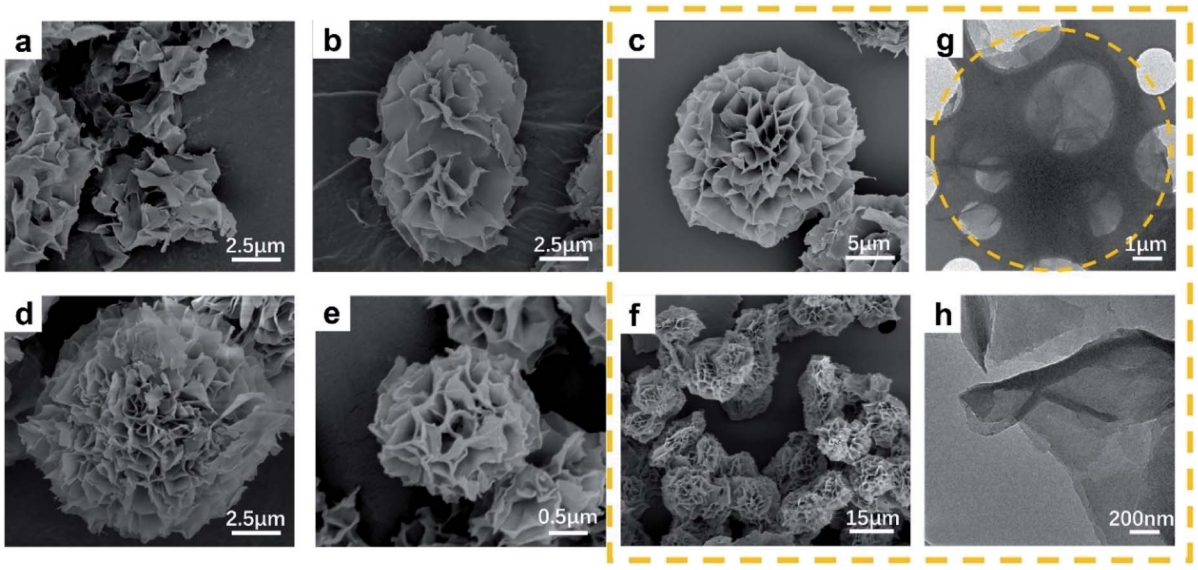

Fig. 4 (a)–(f) SEM images of Cu-TCPP samples synthesized in the presence of (a) 0 μL mL^{-1}, (b) 0.3125 μL mL^{-1}, (c) 0.625 μL mL^{-1}, (d) 0.9375 μL mL^{-1} and (e) 1.25 μL mL^{-1} of TFA. (f) Low-magnification SEM image of C-TCPP synthesized with 0.625 μL mL^{-1} TFA; (g) corresponding TEM image; (h) enlarged TEM image.

(Fig. 2g) of the Cu-TCPP and the starting material $Cu(NO_3)_2 \cdot 3H_2O$ featured $2p_{1/2}$ and $2p_{3/2}$ peaks near 953.5 and 933.5 eV, with their accompanying peaks appearing at the same positions, indicating that the Cu atoms in Cu-TCPP were divalent;[34,35] in other words, the Cu^{2+} ion and TCPP structure underwent coordination without undergoing an oxidation/reduction reaction. The C 1s spectrum (Fig. 2f) of Cu-TCPP featured two distinct peaks representing the C–C/C=C bonds (284.7 eV) and the carboxylate C atoms (288.3 eV) of the organic ligands.[36] The O 1s spectrum (Fig. 2h) of Cu-TCPP contained two characteristic peaks at 531.7 (C–O–Cu) and 532.5 (C–O) eV; the N 1s spectrum (Fig. 2i) displayed peaks at 398.5 and 400.0 eV for the N–Cu and –NH– bonds, respectively. TGA revealed that the decomposition of Cu-TCPP occurred in two stages (Fig. S3†). The first stage of the decomposition of Cu-TCPP occurred at 300–395 °C, with a weight loss of 21.29%, representing the separation of Cu^{2+} ions and TCPP, at this stage, the structure of Cu-TCPP MOFs collapsed; the second occurred in the range from 396 to 545 °C, representing the decomposition of the C species, with a weight loss of 47.28%. Accordingly, the flower-like Cu-TCPP had good thermal stability, decomposition will not occur before 300 °C.

We used SEM to observe the morphologies and structures of the samples of Cu-TCPP synthesized in the presence of the same amount of the various acids (1.25 μL mL^{-1}). The SEM images in Fig. 3a–f reveal that only the addition of TFA led to the synthesis of flower-like Cu-TCPP with complete morphology and uniform size, while the addition of other acids cannot obtain flower-like Cu-TCPP, indicating that TFA is the key factor to control the synthesis of flower-like Cu-TCPP.

We further studied the influence of the concentration of TFA on the morphology of Cu-TCPP. Fig. 4a–e display SEM images of the Cu-TCPP formed in the presence of TFA (0 μL mL^{-1}, 0.3125 μL mL^{-1}, 0.625 μL mL^{-1}, 0.9375 μL mL^{-1} and 1.25 μL mL^{-1}, respectively). Upon increasing the amount of TFA, the flower-like structure became more compact and complete; the average diameter of the generated flowers was 25–30 μm. When the amount of added TFA reached 1.25 μL mL^{-1}, the average diameter of the generated flowers decreased and the petals became thicker. Therefore, the appropriate amount of added TFA appeared to be 0.625 μL mL^{-1}, the resulting Cu-TCPP featured the most complete flower-like structure and an appropriate tightness of the self-assembly. Fig. 4f is a low-magnification SEM image of Cu-TCPP synthesized with 0.625 μL mL^{-1}. Fig. 4g and h is a TEM characterization of Cu-TCPP synthesized with 0.625 μL mL^{-1}. It is found that the light transmitted in the middle position is less, the color is darker, and the edge light transmittance is better, the color is brighter. The TEM image confirmed that the prepared flower-like Cu-TCPP was formed by the assembly and stacking of Cu-TCPP

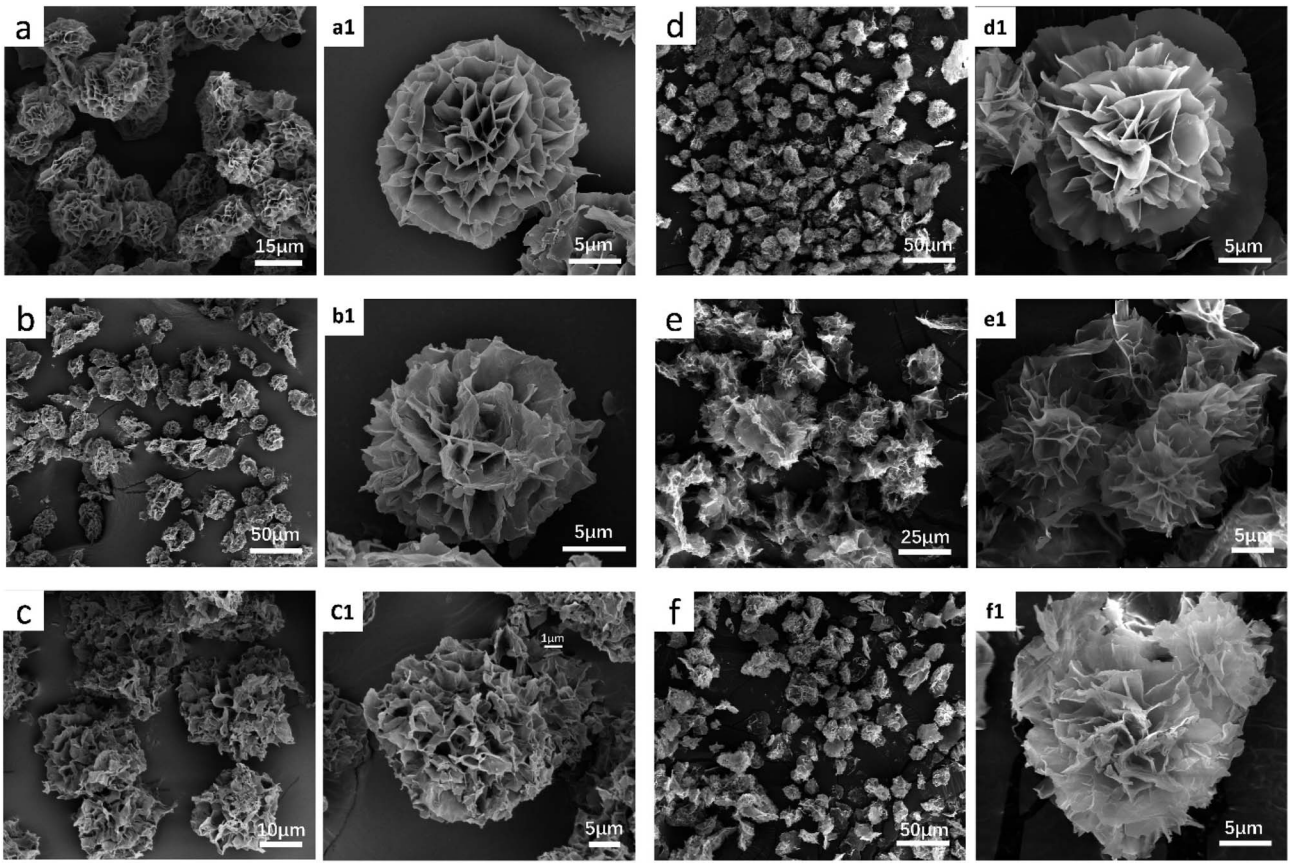

Fig. 5 (a)–(c) SEM images of (a) Cu-TCPP, (b) Zn-TCPP, and (c) Co-TCPP synthesized adding 0.625 μL mL^{-1} of TFA. (d)–(f) SEM images of (d) CuZn-TCPP, (e) ZnCo-TCPP, and (f) CuCo-TCPP. (a1)–(f1) Corresponding enlarged SEM image.

nanosheets. And the circular profile shown by TEM is consistent with the results of SEM.

In order to prove that our method of synthesizing flower-like porphyrin-based MOFs is universally applicable. We synthesized the corresponding MOFs with TCPP as the ligand and Zn^{2+} and Co^{2+} as the metal ions used the same method and also obtained flower-like MOFs. Indeed, when we combined Cu^{2+}, Zn^{2+}, and Co^{2+} in pairs, we obtained bimetallic MOFs with flower-like morphologies again. Fig. 5 displays SEM and TEM images of these MOFs. It shows that our method is not only feasible for Cu-TCPP, but is suitable for the synthesis of other divalent metal porphyrin-based MOFs.

Regarding why the addition of TFA can promote the self-assembly of Cu-TCPP nanosheets into flower shapes, the in-depth mechanism has also aroused our interest. We propose a possible self-assembly mechanism of formation of the flower-like structures based on the formation process, as shown in Fig. 6. Initially, the Cu^{2+} ions matched with TCPP to form MOFs sheet. Due to the highly electronegative CF_3– group in TFA, the negatively charged Cu-TCPP sheets are attracted and stacked together like a folded fan. Then because the Cu-TCPP species were negatively charged, the sheets would repel each other. As the degree of charge repulsion increased, the stacked MOFs sheets gradually like an opened fan; as the reaction time increased, the fan-shaped sheets gradually increased in size and gathered. In the later stages of the reaction, PVP restricted the vertical growth of Cu-TCPP, ensuring that it could continue to grow only horizontally. In the final washing process, the excess reactants and Cu-TCPP fragments on the surface were washed away, resulting in a complete flower shape.

The number of exposed active sites would be a key factor affecting the photocatalytic performance,[37] with a large specific surface area facilitating the exposure of active sites and improving the photocatalytic performance. We used the BET method to measure the specific surface areas and pore structures of the flower-like Cu-TCPP (Fig. 7). We obtained a typical type-IV adsorption isotherm with a hysteresis loop, indicative of the existence of a micro-/mesopore structure.[38] The pore size distribution data were consistent (Fig. 7b). The BET surface area of the flower-like Cu-TCPP synthesized in the presence of TFA was 605.04 $m^2 g^{-1}$, the BET surface area of Cu-TCPP nanosheets is 485 $m^2 g^{-1}$,[33] and the BET surface area of Cu-TCPP powder is 520 $m^2 g^{-1}$.[39] In contrast, the flower-like Cu-TCPP we synthesized has a larger BET surface area, which is due to the nanosheets self-assembled into a flower shape to form mesopores. This shows that self-assembly into flower shape can increase the BET surface area.

3.2 Photocatalytic properties

We used UV-vis absorption spectra to evaluate the photocatalytic performance of the flower-like Cu-TCPP for the degradation of RhB under visible light (>420 nm). When kept in the dark, RhB was removed mainly from the solution through its adsorption onto the flower-like Cu-TCPP; this adsorption/desorption equilibrium was usually reached within 40–60 min. The mixture was then placed under a 300 W Xe lamp

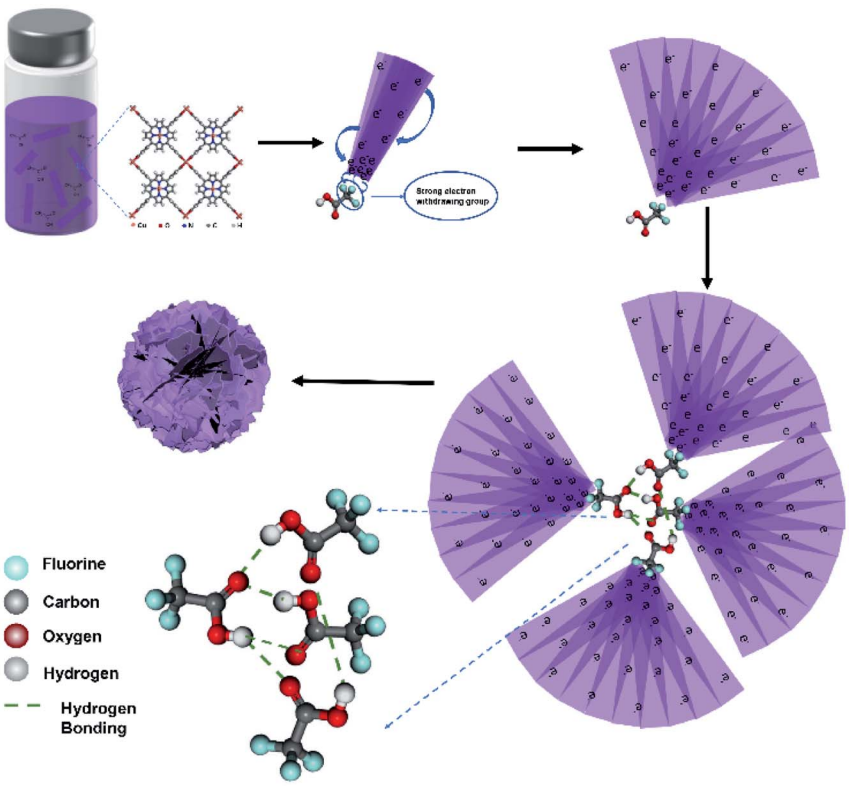

Fig. 6 Mechanism of formation of flower-like Cu-TCPP structures.

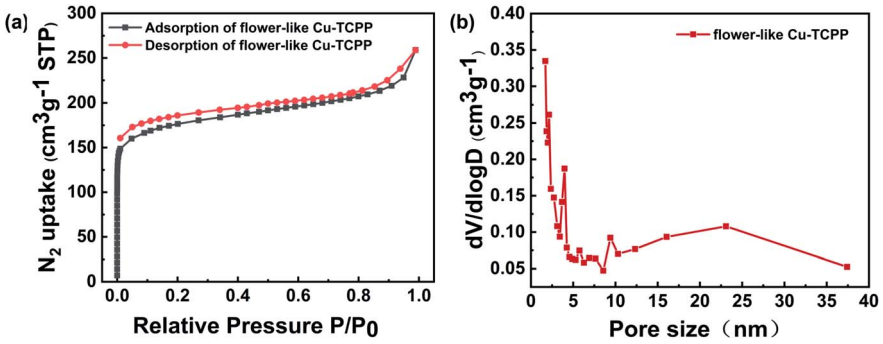

Fig. 7 (a) N_2 adsorption/desorption isotherms of flower-like Cu-TCPP. (b) Corresponding pore size distribution of the flower-like Cu-TCPP, calculated using the model of the full-aperture distribution NLDFT method.

equipped with a 420 nm optical cut-off filter. Samples were collected every 20 min and centrifuged to measure the concentration of the dye.

The pH can significantly affect the surface charge of an adsorbent.[40] Adjust the pH of the flower-like Cu-TCPP aqueous dispersion with 0.1 M HCl and NaOH, and test the zeta potential at different pH. Fig. 8a reveals that as the pH increased, the zeta potential of the flower-like Cu-TCPP suspension decreased, reaching a value of −30.13 mV at pH 11. Because RhB is a cationic dye, negative charge facilitated adsorption on the surface of Cu-TCPP through electrostatic interactions. Hence, a stronger negative charge increased the rate of removal of RhB by Cu-TCPP. Fig. 8b reveals that when the pH reached 11, the removal rate was the highest (47%). Accordingly, we choose the optimal photocatalytic pH to be 11.

The removal efficiency [E (%)] of RhB was calculated using the equation

$$E = \frac{C_0 - C_e}{C_0} \times 100\%$$

where C_0 and C_e are the initial and equilibrium concentrations of RhB, respectively.

In the absence of the flower-like Cu-TCPP photocatalyst, we observed no variation in the concentration of RhB over a 120 min period of irradiation with visible light, confirming the stability of RhB under irradiation. After adding a small amount of H_2O_2 to the RhB solution, the removal efficiency of RhB

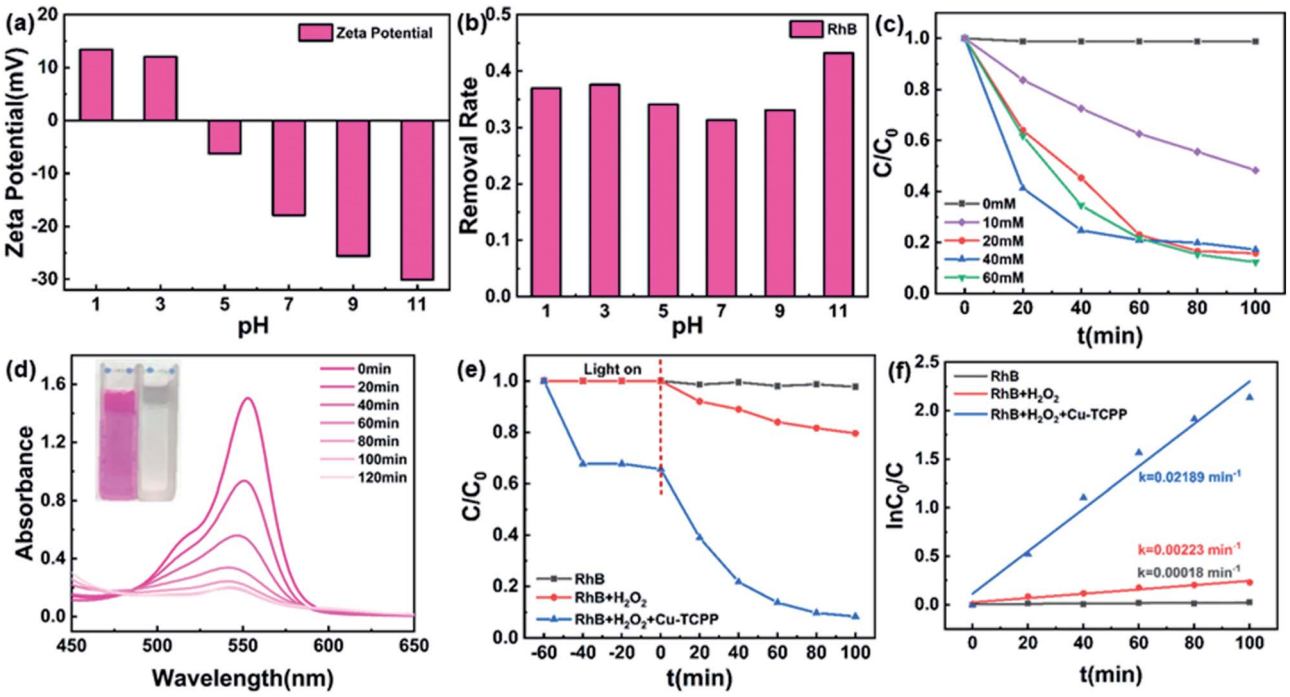

Fig. 8 (a) Zeta potentials of flower-like Cu-TCPP suspensions and (b) removal rates of RhB at various values of pH. (c) Effect of concentration of H_2O_2 on the degradation of RhB; conditions: RhB, 10 ppm; Cu-TCPP, 0.1 g L^{-1}; initial pH 11. (d) UV-vis absorption spectra of RhB recorded at various times during the photocatalytic process. (e) Photocatalytic degradation curve. (f) Plots of ln(C_0/C) with respect to time, providing apparent reaction rate constants (k).

increases to 22% under visible light, presumably because of the photolysis of H_2O_2 to form reactive $^{\bullet}OH$ (H_2O_2 + visible light → $^{\bullet}OH + OH^-$).[5] Experiments performed using various amounts of H_2O_2 additive (Fig. 8d) indicated that the optimal concentration of H_2O_2 was 40 mM. Fig. 8c shows that with the prolongation of the illumination time, the absorbance value of RhB decreases rapidly and the maximum absorption wavelength shifts to shorter wavelengths, which represents the decomposition of RhB. The flower-like Cu-TCPP degraded approximately 88% of the RhB in the presence of 40 mM H_2O_2 within 100 min, the result of Cu-TCPP activating H_2O_2 to form reactive $^{\bullet}OH$ species. Compared with other pure MOFs, the flower-like porphyrin-based MOFs synthesized by us have higher photocatalytic efficiency. *E.g.*, the degradation efficient of 2D Cu-TCPP nanosheets to RhB is 81.2% in 6 hours under visible light,[40] the degradation efficient of MIL-88A(Fe) to RhB is 45% within 80 min under visible light.[5] According to the data in Fig. 8f, during the entire photocatalytic degradation process, the photocatalytic degradation rate constant k of Cu-TCPP for RhB is 2.189×10^{-2} min^{-1}, while the addition of H_2O_2 to RhB is only 2.23×10^{-3} min^{-1}, indicating that flower-like Cu-TCPP has high photocatalytic degradation ability.

3.3 Reusability and stability of flower-like Cu-TCPP

To evaluate the possibility of using this catalyst in practical application, we studied the reusability and stability of the flower-like Cu-TCPP. After the photocatalysis experiment was over, the flower-like Cu-TCPP was centrifuged, washed with ethanol and water for three times, and then put into the next use after freeze-drying, and the cycle is repeated five times. As revealed in Fig. 9, after five repeated uses, the photocatalytic degradation activity of flower-like Cu-TCPP on RhB did not decrease significantly, indicating their high photocatalytic stability and suitability for use in the degradation treatment of RhB dye. In addition, the XRD diffraction patterns (Fig. S4a†) and FTIR spectra (Fig. S4b†) of the flower-like Cu-TCPP recorded before and after the photocatalytic reaction revealed that the crystal structure and surface-active groups of the catalyst had not changed significantly. Furthermore, SEM images (Fig. S5†) recorded before and after use revealed that the flower-like morphology was maintained after photocatalysis, confirming that Cu-TCPP has good stability. Together, these analyses indicate that the flower-like Cu-TCPP were stable in the photocatalytic process and have potential value for practical application.

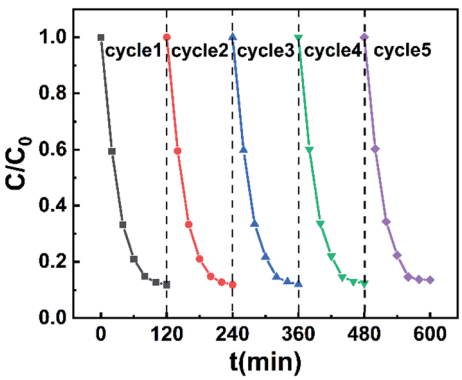

Fig. 9 Reusability of flower-like Cu-TCPP for the photodegradation of RhB.

3.4. Photocatalytic mechanism

To clarify the photocatalytic mechanism, we wished to clarify the active species that played a role in the degradation process. Accordingly, we introduced EDTA-2Na, isopropanol, and *p*-benzoquinone (0.1 mM) as scavengers for holes h^+, $^{\bullet}OH$, and $^{\bullet}O_2^-$, respectively, during the process of removal of RhB under visible light irradiation. Fig. 10 reveals that the degradation rate of RhB was affected in the order EDTA-2Na > *p*-benzoquinone > isopropanol. Therefore, we conclude that h^+, $^{\bullet}O_2^-$ and $^{\bullet}OH$ all play an important role in the photocatalysis process, h^+ and $^{\bullet}O_2^-$ played leading roles in the degradation process.

Using the UV-vis diffuse reflectance spectrum (DRS) to elucidate the optical activities of flower-like Cu-TCPP. The band gap (E_g) of flower-like Cu-TCPP can be calculated as 2.27 eV from Tauc plot of the UV-vis DRS spectrum (Fig. S7†). According to the valence band X-ray photoelectron spectroscopy (VB XPS) measurement (Fig. S8†), the conduction band potential (E_{CB}) of flower-like Cu-TCPP was −0.36 eV *vs.* NHE (normal hydrogen electrode), the valence band potential (E_{VB}) was 1.91 eV *vs.* NHE.

Based on the above data analysis and results, we suggest the following possible mechanism to explain the efficient photocatalytic degradation of RhB in the presence of flower-like Cu-TCPP:

$$\text{Cu-TCPP} + h\nu \rightarrow \text{Cu-TCPP}\,[e^- + h^+]$$

$$O_2 + e^- \rightarrow {}^{\bullet}O_2^-$$

$$H_2O_2 + e- \rightarrow {}^{\bullet}OH + OH^-$$

$$^{\bullet}O_2^- + h^+ + {}^{\bullet}OH + \text{RhB} \rightarrow \text{degradation products}$$

First, the flower-like Cu-TCPP absorbed visible light and produced holes (h^+) and electrons (e^-). The h^+ have oxidizing

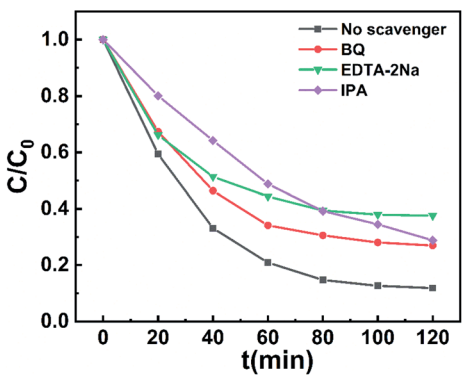

Fig. 10 Effects of various scavengers on the photodegradation of RhB mediated by flower-like Cu-TCPP under irradiation with visible light. Experimental conditions: RhB, 10 mg L^{-1}; H_2O_2, 40 mM; flower-like Cu-TCPP, 0.1 g L^{-1}; initial pH 11.

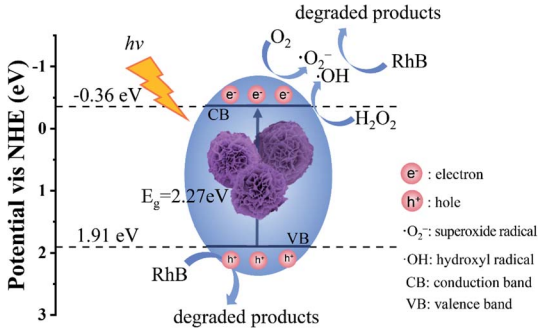

Fig. 11 Reasonable mechanism for the process of photocatalytic degradation of RhB mediated by flower-like Cu-TCPP.

ability and the redox potential of RhB is about 1.43 eV *vs.* NHE, it is significantly lower than the valence band potential E_{VB} (1.91 eV *vs.* NHE) of flower-like Cu-TCPP, therefore, the photogenerated holes (h^+) in the valence band of flower-like Cu-TCPP can directly oxidize and degrade RhB. Because the conduction band potential E_{CB} (−0.36 eV *vs.* NHE) of flower-like Cu-TCPP was more negative than the standard redox potential of $O_2/{}^{\bullet}O_2^-$ (−0.33 eV *vs.* NHE),[41] so the accumulated e^- in the conduction band reacted with O_2 to generate superoxide radicals (${}^{\bullet}O_2^-$). Meanwhile, the H_2O_2 consumed e^- to product hydroxyl radicals (${}^{\bullet}OH$) and enhanced the separation of photogenerated electrons and holes,[5] which is beneficial to photocatalytic reactions. Therefore, under the combined action of ${}^{\bullet}O_2^-$, ${}^{\bullet}OH$ and h^+, RhB was degraded. Fig. 11 displays the specific mechanism.

4. Conclusions

By adding TFA as a morphological control agent in solvothermal method, we have obtained flower-like porphyrin-based MOFs self-assembled from nanosheets. The optimal amount of added TFA was 0.625 μL mL^{-1}, the resulting flower-like Cu-TCPP had the most complete and uniform morphology and has a larger BET surface area. Because of the self-assembly of nanosheets, the stability and reusability of the flower-like porphyrin MOFs were excellent. In addition, this flower-like Cu-TCPP displayed excellent photosensitivity, when applied to the photocatalytic degradation of the cationic dye RhB, the degradation efficient reached 88% within 100 min. Compared with other pure MOFs materials, the time required to achieve the same degradation effect is reduced. Through the free radical trapping reaction, the results prove that the photocatalytic degradation reaction is caused by the flower-like Cu-TCPP producing h^+, ${}^{\bullet}O_2^-$, and ${}^{\bullet}OH$ species in the system. Furthermore, the method we developed to synthesize flower-like porphyrin-based MOFs by adding TFA as a morphology control agent has made a great contribution to the precise control of morphology, this method can be extended to control the morphology of other MOFs.

Conflicts of interest

The authors declare no competing financial interest.

Acknowledgements

We thank the National Natural Science Foundation of China (grant 21878089) for financial support.

References

1 I. Nath, J. Chakraborty, P. M. Heynderickx and F. Verpoort, Engineered synthesis of hierarchical porous organic polymers for visible light and natural sunlight induced rapid degradation of azo, thiazine and fluorescein based dyes in a unique mechanistic pathway, *Appl. Catal., B*, 2018, **227**, 102–113.

2 Z. Hasan and S. H. Jhung, Removal of hazardous organics from water using metal–organic frameworks (MOFs): plausible mechanisms for selective adsorptions, *J. Hazard. Mater.*, 2015, **283**, 329–339.

3 L. Zhao, Y. Zhao, R. Li, D. Wu, X. Xie, H. Ye, Y. Zhang and Q. Xin, Insights into the binding mechanism of 2D copper-tetrakis-(4-carboxyphenyl)-porphyrin metal–organic framework nanosheets with rhodamine B: spectroscopic and thermodynamics studies, *Chem. Phys.*, 2020, **534**, 110743.

4 H. K. Melvin Ng, C. P. Leo and A. Z. Abdullah, Selective removal of dyes by molecular imprinted TiO_2 nanoparticles in polysulfone ultrafiltration membrane, *J. Environ. Chem. Eng.*, 2017, **5**, 3991–3998.

5 N. Liu, W. Huang, X. Zhang, L. Tang, L. Wang, Y. Wang and M. Wu, Ultrathin graphene oxide encapsulated in uniform MIL-88A(Fe) for enhanced visible light-driven photodegradation of RhB, *Appl. Catal., B*, 2018, **221**, 119–128.

6 C. X. Liu, W. H. Zhang, N. Wang, P. Guo, M. Muhler, Y. Wang, S. Lin, Z. Chen and G. Yang, Highly efficient photocatalytic degradation of dyes by a copper-triazolate metal–organic framework, *Chem.–Eur. J.*, 2018, **24**, 16804–16813.

7 Y. Gao, S. Li, Y. Li, L. Yao and H. Zhang, Accelerated photocatalytic degradation of organic pollutant over metal–organic framework MIL-53(Fe) under visible LED light mediated by persulfate, *Appl. Catal., B*, 2017, **202**, 165–174.

8 S. Rojas and P. Horcajada, Metal–organic frameworks for the removal of emerging organic contaminants in water, *Chem. Rev.*, 2020, **120**, 8378–8415.

9 P. Mahata, G. Madras and S. Natarajan, Novel photocatalysts for the decomposition of organic dyes based on metal–organic framework compounds, *J. Phys. Chem. B*, 2006, **110**, 13759–13768.

10 H. Yang, X. W. He, F. Wang, Y. Kang and J. Zhang, Doping copper into ZIF-67 for enhancing gas uptake capacity and visible-light-driven photocatalytic degradation of organic dye, *J. Mater. Chem.*, 2012, **22**, 21849–21851.

11 S. R. Batten, N. R. Champness, X. M. Chen, J. Garcia-Martinez, S. Kitagawa, L. Öhrström, M. O'keeffe, M. P. Suh and J. Reedijk, Terminology of metal–organic frameworks and coordination polymers (IUPAC Recommendations 2013), *Pure Appl. Chem.*, 2013, **85**, 1715–1724.

12 L. Jiao, Y. Wang, H. L. Jiang and Q. Xu, Metal–organic frameworks as platforms for catalytic applications, *Adv. Mater.*, 2018, **30**, 1703663.
13 Y. R. Lee, J. Kim and W. S. Ahn, Synthesis of metal–organic frameworks: a mini review, *Korean J. Chem. Eng.*, 2013, **30**, 1667–1680.
14 L. Zeng, X. Guo, C. He and C. Duan, Metal–organic frameworks: versatile materials for heterogeneous photocatalysis, *ACS Catal.*, 2016, **6**, 7935–7947.
15 Y. Zhou, W. Yang, M. Qin and H. Zhao, Self-assembly of metal–organic framework thin films containing metalloporphyrin and their photocatalytic activity under visible light, *Appl. Organomet. Chem.*, 2016, **30**, 188–192.
16 J. Guo, Y. Wan, Y. Zhu, M. Zhao and Z. Tang, Advanced photocatalysts based on metal nanoparticle/metal–organic framework composites, *Nano Res.*, 2020, DOI: 10.1007/s12274-020-3182-1.
17 L. Jiao, J. Y. R. Seow, W. S. Skinner, Z. U. Wang and H. L. Jiang, Metal–organic frameworks: structures and functional applications, *Mater. Today*, 2019, **27**, 43–68.
18 Y. Z. Chen, Z. U. Wang, H. Wang, J. Lu, S. H. Yu and H. L. Jiang, Singlet oxygen-engaged selective photo-oxidation over pt nanocrystals/porphyrinic MOF: the roles of photothermal effect and pt electronic state, *J. Am. Chem. Soc.*, 2017, **139**, 2035–2044.
19 J. D. Xiao and H. L. Jiang, Metal–organic frameworks for photocatalysis and photothermal catalysis, *Acc. Chem. Res.*, 2019, **52**, 356–366.
20 F. Guo, Y. P. Wei, S. Q. Wang, X. Y. Zhang, F. M. Wang and W. Y. Sun, Pt nanoparticles embedded in flowerlike NH_2-UiO-68 for enhanced photocatalytic carbon dioxide reduction, *J. Mater. Chem. A*, 2019, **7**, 26490–26495.
21 H. Q. Xu, J. Hu, D. Wang, Z. Li, Q. Zhang, Y. Luo, S. H. Yu and H. L. Jiang, Visible-light photoreduction of CO_2 in a metal–organic framework: boosting electron–hole separation via electron trap states, *J. Am. Chem. Soc.*, 2015, **137**, 13440–13443.
22 N. Heidary, M. Morency, D. Chartrand, K. H. Ly, R. Iftimie and N. Kornienko, Electrochemically triggered dynamics within a hybrid metal–organic electrocatalyst, *J. Am. Chem. Soc.*, 2020, **142**, 12382–12393.
23 F. Leng, H. Liu, M. Ding, Q. P. Lin and H. L. Jiang, Boosting photocatalytic hydrogen production of porphyrinic MOFs: the metal location in metalloporphyrin matters, *ACS Catal.*, 2018, **8**, 4583–4590.
24 A. Fateeva, P. A. Chater, C. P. Ireland, A. A. Tahir, Y. Z. Khimyak, P. V. Wiper, J. R. Darwent and M. J. Rosseinsky, A water-stable porphyrin-based metal–organic framework active for visible-light photocatalysis, *Angew. Chem., Int. Ed.*, 2012, **51**, 7440–7444.
25 J. Park, D. Feng, S. Yuan and H. C. Zhou, Photochromic metal–organic frameworks: reversible control of singlet oxygen generation, *Angew. Chem., Int. Ed. Engl.*, 2015, **54**, 440–445.
26 D. Feng, Z. Y. Gu, J. R. Li, H. L. Jiang, Z. Wei and H. C. Zhou, Zirconium-metalloporphyrin PCN-222: mesoporous metal–organic frameworks with ultrahigh stability as biomimetic catalysts, *Angew. Chem., Int. Ed.*, 2012, **51**, 10307–10310.
27 G. Li, X. Zhang, H. Zhang, C. Liao and G. Jiang, Bottom-up MOF-intermediated synthesis of 3D hierarchical flower-like cobalt-based homobimetallic phosphide composed of ultrathin nanosheets for highly efficient oxygen evolution reaction, *Appl. Catal., B*, 2019, **249**, 147–154.
28 S. Zheng, B. Li, Y. Tang, Q. Li, H. Xue and H. Pang, Ultrathin nanosheet-assembled $[Ni_3(OH)_2(PTA)_2(H_2O)_4]\cdot 2H_2O$ hierarchical flowers for high-performance electrocatalysis of glucose oxidation reactions, *Nanoscale*, 2018, **10**, 13270–13276.
29 Z. M. Cui, Z. Chen, C. Y. Cao, W. G. Song and L. Jiang, Coating with mesoporous silica remarkably enhances the stability of the highly active yet fragile flower-like MgO catalyst for dimethyl carbonate synthesis, *Chem. Commun.*, 2013, **49**, 6093–6095.
30 S. Zhang, L. Li, S. Zhao, Z. Sun, M. Hong and J. Luo, Hierarchical metal–organic framework nanoflowers for effective CO_2 transformation driven by visible light, *J. Mater. Chem. A*, 2015, **3**, 15764–15768.
31 C. C. Hou, L. Zou and Q. Xu, A Hydrangea-like superstructure of open carbon cages with hierarchical porosity and highly active metal sites, *Adv. Mater.*, 2019, **31**, 1904689.
32 M. Zhao, Y. Wang, Q. Ma, Y. Huang, X. Zhang, J. Ping, Z. Zhang, Q. Lu, Y. Yu, H. Xu, Y. Zhao and H. Zhang, Ultrathin 2D metal–organic framework nanosheets, *Adv. Mater.*, 2015, **27**, 7372–7378.
33 G. Xu, K. Otsubo, T. Yamada, S. Sakaida and H. Kitagawa, Superprotonic conductivity in a highly oriented crystalline metal–organic framework nanofilm, *J. Am. Chem. Soc.*, 2013, **135**, 7438–7441.
34 L. Wang, S. Duan, P. Jin, H. She, J. Huang, Z. Lei, T. Zhang and Q. Wang, Anchored Cu(II) tetra(4-carboxylphenyl) porphyrin to P25 (TiO_2) for efficient photocatalytic ability in CO_2 reduction, *Appl. Catal., B*, 2018, **239**, 599–608.
35 B. Li, X. Wang, L. Chen, Y. Zhou, W. Dang, J. Chang and C. Wu, Ultrathin Cu-TCPP MOF nanosheets: a new theragnostic nanoplatform with magnetic resonance/near-infrared thermal imaging for synergistic phototherapy of cancers, *Theranostics*, 2018, **8**, 4086–4096.
36 Y. Yue, J. Yi, L. Wang and J. Feng, Toward a more comprehensive understanding on the structure evolution and assembly formation of a bisamide nucleating agent in polypropylene melt, *Macromolecules*, 2020, **53**, 4381–4394.
37 Y. Li, M. Lu, P. He, Y. Wu, J. Wang, D. Chen, H. Xu, J. Gao and J. Yao, Bimetallic metal–organic framework-derived nanosheet-assembled nanoflower electrocatalysts for efficient oxygen evolution reaction, *Chem.–Asian J.*, 2019, **14**, 1590–1594.
38 W. Xuan, C. Zhu, Y. Liu and Y. Cui, Mesoporous metal–organic framework materials, *Chem. Soc. Rev.*, 2012, **41**, 1677–1695.
39 D. T. Lee, J. D. Jamir, G. W. Peterson and G. N. Parsons, Water-stable chemical-protective textiles via euhedral

surface-oriented 2D Cu-TCPP metal–organic frameworks, *Small*, 2019, **15**, 1805133.

40 S. Zhao, S. Li, Z. Zhao, Y. Su, Y. Long, Z. Zheng, D. Cui, Y. Liu, C. Wang, X. Zhang and Z. Zhang, Microwave-assisted hydrothermal assembly of 2D copper-porphyrin metal–organic frameworks for the removal of dyes and antibiotics from water, *Environ. Sci. Pollut. Res.*, 2020, **27**, 39186–39197.

41 Y. Wang, J. Wang, B. Du, Y. Wng, Y. Xiong, Y. Yang and X. Zhang, Synthesis of hierarchically porous perovskite-carbon aerogel composite catalysts for the rapid degradation of fuchsin basic under microwave irradiation and an insight into probable catalytic mechanism, *Appl. Surf. Sci.*, 2018, **439**, 475–487.